GEOPHYSICS, VOL. 84, NO. 4 (JULY-AUGUST 2019); P. G41–G54, 11 FIGS., 3 TABLES.
10.1190/GEO2018-0491.1

Three-dimensional numerical modeling of gravity and magnetic anomaly in a mixed space-wavenumber domain

Shikun Dai[1], Dongdong Zhao[1], Shunguo Wang[2], Bin Xiong[3], Qianjiang Zhang[1], Kun Li[1], Longwei Chen[3], and Qingrui Chen[1]

ABSTRACT

Fast and accurate numerical modeling of gravity and magnetic anomalies is the basis of field-data inversion and quantitative interpretation. In gravity and magnetic prospecting, the computation and memory requirements of practical modeling is still a significant issue, which leads to the difficulty of using efficient and detailed inversions for large-scale complex models. A new 3D numerical modeling method for gravity and magnetic anomaly in a mixed space-wavenumber domain is proposed to mitigate the difficulties. By performing a 2D Fourier transform along two horizontal directions, 3D partial differential equations governing gravity and magnetic potentials in the spatial domain are transformed into a group of independent 1D differential equations wrapped with different wavenumbers. Importantly, the computation and memory requirements of modeling are greatly reduced by this method. A modeling example with 4,040,100 observations can be finished in approximately 28 s on a desktop using a single core, and the independent differential equations are highly parallel among different wavenumbers. The method preserves the vertical component in the space domain, and thus a mesh for modeling can be finer at a shallower depth and coarser at a deeper depth. In general, the new method takes into account the calculation accuracy and the efficiency. The finite-element algorithm combined with a chasing method is used to solve the transformed differential equations with different wavenumbers. In a synthetic test, a model with prism-shaped anomalies is used to verify the accuracy and efficiency of the proposed algorithm by comparing the analytical solution, our numerical solution, and a well-known numerical solution. Furthermore, we have studied the balance between computational accuracy and efficiency using a standard fast Fourier transform (FFT) method with grid expansion and the Gauss-FFT method. A model with topography is also used to explore the ability of modeling topography with our method. The results indicate that the proposed method using the Gauss-FFT method has characteristics of fast calculation speed and high accuracy.

INTRODUCTION

Gravity and magnetics are well-known methods in geophysical explorations (Blakely, 1996). Recently, they have increasingly been applied in mineral exploration (Nabighian et al., 2005; Mosher and Farquharson, 2013; Kamm et al., 2015), delineation of deep geologic structures (Saleh et al., 2006; Prutkina and Salehb, 2009; Dutra et al., 2012; Aitken et al., 2013), and engineering and environmental problems (Zunino et al., 2009; Eppelbaum, 2011; Rim and Li, 2012; Pedersen and Bastani, 2016). Highly efficient and accurate gravity and magnetic methods for large-scale investigations have consistently been given attention due to the difficulties in exploration at a couple of kilometer depth, especially under complex geologic conditions. The numerical modeling of the gravity and magnetic fields seems particularly important as a fundamental tool for improving inverse imaging and high-quality interpretation (Blakely, 1996; Li and Oldenburg, 1996, 1998).

Manuscript received by the Editor 28 June 2018; revised manuscript received 7 March 2019; published ahead of production 8 May 2019; published online 19 June 2019.
[1]Central South University, Key Laboratory of Metallogenic Prediction of Nonferrous Metals and Geological Environment Monitoring, Ministry of Education, Changsha, China and Central South University, School of Geosciences and Info-physics, Changsha, China. E-mail: dskgmes@csu.edu.cn; dongzhaochd@163.com; 359963349@qq.com; 546803024@qq.com; 1532550316@qq.com.
[2]Scripps Institution of Oceanography, UC San Diego, La Jolla, California, USA. E-mail: s4wang@ucsd.edu; wangshunguo@yeah.net (corresponding author).
[3]Guilin University of Technology, College of Earth Sciences, Guilin, China. E-mail: xiongbin@glut.edu.cn; 89585040@qq.com.

The forward modeling of gravity and magnetic anomalies are mainly cataloged into two types: (1) spatial-domain and (2) Fourier-domain methods. Methods in both categories have been developed to model anomalies caused by different types of sources. The spatial-domain methods can further be divided into analytical methods and numerical methods. The analytical methods are more accurate and straightforward to model anomalies by closed-form equations. For examples, explicit expressions for horizontal thin plate with arbitrary polygon (Talwani, 1960) and rectangle (Bhattacharyya, 1964; Nagy, 1966), polyhedron with a triangle as surface (Paul, 1974), vertical prism with arbitrary side faces (Plouff, 1976), and vertical cylinder (Singh and Sabina, 1978) were studied at early time. Later, studies have focused on formula deduction and simplification for complex 3D models (Barnett, 1976; Okabe, 1979; Furness, 1994; Li and Chouteau, 1998; Singh and Guptasarma, 2001; Chakravarthi et al., 2002; Holstein, 2002; García-Abdeslem, 2005; Zhang and Jiang, 2017), singular point processing by analytic integral (Kwok, 1991), the boundary field continuity problem (Li and Chouteau, 1998; Nagy et al., 2000), and the general solution for a polyhedral body with quadratic density contrast (Ren et al., 2017a, 2018). An adaptive multilevel fast method has also been developed to save the gravity and magnetic modeling time (Ren et al., 2017b). However, the applications are restricted by the complexity of expressions, large computational costs, and, at most times, restricted application of the analytical expressions. The numerical methods involved in gravity and magnetic modeling are mainly finite-difference (Farquharson and Mosher, 2009), finite-volume (Lelièvre, 2003; Lelièvre and Oldenburg, 2006; Jahandari and Farquharson, 2013; Guzman, 2015), finite-element (Cai and Wang, 2005; Jahandari and Farquharson, 2013; Maag et al., 2017), and differential-equation (Haber et al., 2014) methods to obtain the solution of the Poisson equation related to scalar potentials or fields. Particularly, when the source elements and/or observation sites are numerous, the computational cost of forward modeling can still be a serious issue for 3D inversion.

Fourier-domain methods calculate gravity and magnetic anomalies in Fourier domain, then use inverse Fourier transform to obtain anomaly fields. These Fourier-domain methods show relatively high efficiency due to straightforward expressions of the anomaly fields in the Fourier domain. For examples Bhattacharyya (1966) deduces the spectral expression of magnetic fields for arbitrary magnetization, Parker (1972) calculates gravity and magnetic anomaly by a sum of Fourier transforms, and Pedersen (1978a, 1978b) shows the expressions of vertical cylinder and polyhedron model in Fourier domain, respectively. Xiong (1984) evaluates the expression of the 3D gravitational potential in the Fourier domain for a cuboid model. Much additional research has been carried out on deriving analytic expressions in the Fourier domain for continuous variation of physical property in models (Wu, 1983; Pedersen, 1985; Feng, 1986; Granser, 1987; Zhao and Yedlin, 1991; Rao et al., 1993; Chai, 1997), on expressions of the Parker model in the Fourier domain (Forsberg, 1985), and on the offset-sampling method (Chai, 1997). Later, the fast Fourier transform (FFT) method was introduced in gravity modeling. Tontini et al. (2009) develop a fast forward modeling method for the potential field anomalies generated by complex 3D sources using 3D FFT, and study the errors of the standard FFT method with grid expansion. Phillips et al. (2008) use Markov perturbation of an initial density model to do inversion. Wu and Tian (2014) and Wu and Chen (2016) use Gauss FFT to improve the accuracy of the inverse Fourier transform and reduce the influence of the forced periodicity and the truncation errors caused by the FFT method.

Recently, Fourier-domain methods have gradually been replacing space-domain methods as the primary option for large-scale, complex 3D gravity and magnetic modeling due to its simplicity, accuracy, and efficiency. Particularly, for gravity and magnetic methods, computation and storage memory requirements for a practical numerical modeling in the space or Fourier domain are high, which leads to the difficulty of efficiently using detailed inversions requiring large-scale complex models. In this paper, we propose a 3D highly efficient and accurate numerical modeling method for gravity and magnetic anomalies in a mixed space-wavenumber domain. This method converts 3D PDEs in the spatial domain into a group of independent 1D ordinary differential equations by performing a 2D Fourier transform along horizontal directions. By this method, the computation and memory requirements of modeling are greatly reduced and the independent ordinary differential equations are highly parallel in term of wavenumbers because each equation contains different wavenumbers. The method preserves the vertical direction in the spatial domain; thus, the shallow and the deep meshes for modeling can be fine and coarse, respectively. By this way, the accuracy and the efficiency of calculation are taken into account. In our study, the finite-element method is used to solve the transformed differential equations wrapped with different wavenumbers and the efficiency of solving the linear equation system with a fixed bandwidth is improved by a chasing method. In synthetic tests, a model containing a few prisms is used to verify the accuracy and efficiency of the proposed method by comparisons between numerical and analytical or classical solutions. Also, a simple model with undulated observational surface is used to show the ability of modeling topography. In addition, we have also compared the accuracy and the efficiency of modeling between using the standard FFT method with grid expansion and using the Gaussian FFT method.

METHODS

Basic theory

The gravitational potential that satisfies the Poisson equation (Blakely, 1996) can be described as

$$\nabla^2 U^g(x,y,z) = -4\pi G\rho(x,y,z), \tag{1}$$

where U^g presents the gravitational potential in the spatial domain; $G = 6.674 \times 10^{-11}$ N $\cdot$ m^3/kg^2 is Newton's gravitational constant; and $\rho(x,y,z)$ is the residual density; and x, y, and z represent the directions in the Cartesian coordinate system. The CGMS unit system is often used in gravity prospecting, and the unit of the gravity field is mGal. Thus, the unit of gravity field in this paper is transformed into mGal through the relationship of 1 m/s^2 $= 10^5$ mGal.

The magnetic potential is similar to the gravitational potential. The magnetic potential of the weak magnetic body (Blakely, 1996) satisfies

$$\nabla^2 U^m(x,y,z) = \nabla \cdot \mathbf{m}(x,y,z), \tag{2}$$

where U^m is the magnetic potential in the spatial domain and $\mathbf{m}(x,y,z)$ is the magnetization. The CGMS unit system is also generally used in magnetic prospecting. The unit of the magnetic field

is Oe, and its fractional unit is gamma. However, the unit of the magnetic field in this paper is transformed into nT through the relationship of $1\gamma = 10^{-5}\text{Oe} = 1$ nT.

For convenience, the gravity and magnetic potential problem can be written as

$$\nabla^2 U(x, y, z) = f(x, y, z), \tag{3}$$

where U represents either gravity or magnetic potential, and f is equal to $-4\pi G\rho$ and $\nabla \cdot \mathbf{m}$ for the gravity and magnetic potentials, respectively. Transforming equation 3 into the mixed space-wavenumber domain by the 2D Fourier transform along the lateral x- and y-directions gives

$$\frac{\partial^2 \tilde{U}(k_x, k_y, z)}{\partial z^2} - k^2 \tilde{U}(k_x, k_y, z) = \tilde{f}(k_x, k_y, z), \tag{4}$$

where $k = \sqrt{k_x^2 + k_y^2}$. For the gravitational potential, we have

$$\tilde{f}(k_x, k_y, z) = -4\pi G\tilde{\rho}. \tag{5}$$

And, for the magnetic potential, we have

$$\tilde{f}(k_x, k_y, z) = ik_x\tilde{M}_x + ik_y\tilde{M}_y + \frac{\partial \tilde{M}_z}{\partial z}, \tag{6}$$

where $\tilde{U}(k_x, k_y, z)$ represents either gravity or magnetic potential in the mixed domain, $\tilde{\rho}(k_x, k_y, z)$ is the residual density in the mixed domain, $\tilde{M}_x$, $\tilde{M}_y$, and $\tilde{M}_z$ are the magnetizations in the mixed domain, i is the imaginary unit, and k_x and k_y are the wavenumbers in the directions of x and y, respectively.

Interestingly, equation 4 can be decoupled into a group of independent differential equations with respect to different wavenumbers after 2D Fourier transform in the horizontal directions. In this way, a large-scale problem is able to be simplified into a group of small-scale problems that can be treated independently. The meshes can be fine and coarse along the vertical direction in the spatial domain, and it avoids the unnecessary uniformly spaced grid schemes. Besides, a chasing method is used to solve the linear equations with a fixed bandwidth to further improve the computation efficiency. The proposed method dramatically reduces the requirements of storage memory and computation cost and is suitable to the modeling of complex anomalies with the influence of topography. The observation sites must be situated at the grid nodes, or they are obtained by interpolation in practice, and the complex topography and source targets may not be exactly modeled by the method. However, this shortcoming can be mitigated if a fine mesh is used with the price of increasing computation. The method cannot directly solve the problems when the observations are made outside the sources because the observation domain of the gravity or magnetic field and the source domain of the density and magnetization distribution are identical.

Boundary conditions

In a source-free region, the general solution of equation 4 can be written as

$$\tilde{U} = Ae^{kz} + Be^{-kz}, \tag{7}$$

where A and B are the arbitrary constants.

The upper and lower vertical boundaries have different terms in equation 7. Taking a derivative with respect to z on equation 7, there is only one term left in the basic solution of the gravity field or magnetic field depending on which direction will satisfy the zero value of the field. No source is located beyond the upper and lower vertical boundaries so that the boundary conditions used in the modeling are presented in equations 8 and 9 (Ward and Hohmann, 1988)

$$\left.\frac{\partial \tilde{U}}{\partial z}\right|_{z=z_{\min}} = k\tilde{U}, \tag{8}$$

$$\left.\frac{\partial \tilde{U}}{\partial z}\right|_{z=z_{\max}} = -k\tilde{U}, \tag{9}$$

where $z_{\min}$ and $z_{\max}$ are the upper and lower boundaries, respectively, in the Cartesian coordinate system (Figure 1).

Potential, fields, and gradient of fields

The gravitational potential in the mixed space-wavenumber domain can be obtained by solving the ordinary differential equation 4 under the boundary conditions of equations 8 and 9. The gravity field $\mathbf{g}$ in the spatial domain then can be obtained by (Blakely, 1996)

$$\mathbf{g} = \begin{bmatrix} g_x \\ g_y \\ g_z \end{bmatrix} = \begin{bmatrix} \frac{\partial U^g}{\partial x} \\ \frac{\partial U^g}{\partial y} \\ \frac{\partial U^g}{\partial z} \end{bmatrix}. \tag{10}$$

The gravity gradient tensor can be calculated by

$$\mathbf{T_g} = \begin{bmatrix} T^g_{xx} & T^g_{xy} & T^g_{xz} \\ T^g_{yx} & T^g_{yy} & T^g_{yz} \\ T^g_{zx} & T^g_{zy} & T^g_{zz} \end{bmatrix} = \begin{bmatrix} \frac{\partial g_x}{\partial x} & \frac{\partial g_x}{\partial y} & \frac{\partial g_x}{\partial z} \\ \frac{\partial g_y}{\partial x} & \frac{\partial g_y}{\partial y} & \frac{\partial g_y}{\partial z} \\ \frac{\partial g_z}{\partial x} & \frac{\partial g_z}{\partial y} & \frac{\partial g_z}{\partial z} \end{bmatrix}. \tag{11}$$

Therefore, using the Fourier transform on equations 10 and 11, the gravitational potential, fields, and their gradient tensors in the mixed space-wavenumber domain should satisfy

$$\tilde{\mathbf{g}} = \begin{bmatrix} \tilde{g}_x \\ \tilde{g}_y \\ \tilde{g}_z \end{bmatrix} = \begin{bmatrix} ik_x\tilde{U}^g \\ ik_y\tilde{U}^g \\ -Ck\tilde{U}^g \end{bmatrix}, \tag{12}$$

$$\begin{aligned} \tilde{\mathbf{T}}_\mathbf{g} &= \begin{bmatrix} \tilde{T}^g_{xx} & \tilde{T}^g_{xy} & \tilde{T}^g_{xz} \\ \tilde{T}^g_{yx} & \tilde{T}^g_{yy} & \tilde{T}^g_{yz} \\ \tilde{T}^g_{zx} & \tilde{T}^g_{zy} & \tilde{T}^g_{zz} \end{bmatrix} \\ &= \begin{bmatrix} -k_x^2\tilde{U}^g & -k_xk_y\tilde{U}^g & -iCk_xk\tilde{U}^g \\ -k_xk_y\tilde{U}^g & -k_y^2\tilde{U}^g & -iCk_yk\tilde{U}^g \\ -iCk_xk\tilde{U}^g & -iCk_yk\tilde{U}^g & k^2\tilde{U}^g \end{bmatrix}, \end{aligned} \tag{13}$$

where $\tilde{U}^g$, $\tilde{\mathbf{g}}$, and $\tilde{\mathbf{T}}_\mathbf{g}$ represent the gravitational potential, field, and gradient tensor in the mixed domain, respectively, C represents a sign function shown as $\text{sign}(z-z') = \begin{cases} 1 & z \geq z' \\ -1 & z < z' \end{cases}$, where z' is the vertical coordinate of the density model, and z is the vertical coordinate of an observational surface.

The magnetic potential and magnetic induction $\mathbf{b}$ in the spatial domain satisfy (Blakely, 1996)

$$\mathbf{b} = \begin{bmatrix} b_x \\ b_y \\ b_z \end{bmatrix} = -\begin{bmatrix} \frac{\partial U^m}{\partial x} \\ \frac{\partial U^m}{\partial y} \\ \frac{\partial U^m}{\partial z} \end{bmatrix}. \tag{14}$$

The magnetic gradient tensor $\mathbf{T_m}$ can be written into

$$\mathbf{T_m} = \begin{bmatrix} T^m_{xx} & T^m_{xy} & T^m_{xz} \\ T^m_{yx} & T^m_{yy} & T^m_{yz} \\ T^m_{zx} & T^m_{zy} & T^m_{zz} \end{bmatrix} = \begin{bmatrix} \frac{\partial b_x}{\partial x} & \frac{\partial b_x}{\partial y} & \frac{\partial b_x}{\partial z} \\ \frac{\partial b_y}{\partial x} & \frac{\partial b_y}{\partial y} & \frac{\partial b_y}{\partial z} \\ \frac{\partial b_z}{\partial x} & \frac{\partial b_z}{\partial y} & \frac{\partial b_z}{\partial z} \end{bmatrix}. \tag{15}$$

Similar to the gravity derivations above, using the Fourier transform on equations 14 to 15, the magnetic potential, magnetic induction, and its gradient tensor in the mixed space-wavenumber domain satisfy the following:

$$\tilde{\mathbf{b}} = \begin{bmatrix} \tilde{b}_x \\ \tilde{b}_y \\ \tilde{b}_z \end{bmatrix} = -\begin{bmatrix} ik_x\tilde{U}^m \\ ik_y\tilde{U}^m \\ -Ck\tilde{U}^m \end{bmatrix}, \tag{16}$$

$$\begin{aligned} \tilde{\mathbf{T}}_\mathbf{m} &= \begin{bmatrix} \tilde{T}^m_{xx} & \tilde{T}^m_{xy} & \tilde{T}^m_{xz} \\ \tilde{T}^m_{yx} & \tilde{T}^m_{yy} & \tilde{T}^m_{yz} \\ \tilde{T}^m_{zx} & \tilde{T}^m_{zy} & \tilde{T}^m_{zz} \end{bmatrix} \\ &= \begin{bmatrix} k_x^2\tilde{U}^m & k_xk_y\tilde{U}^m & iCk_xk\tilde{U}^m \\ k_xk_y\tilde{U}^m & k_y^2\tilde{U}^m & iCk_yk\tilde{U}^m \\ iCk_xk\tilde{U}^m & iCk_yk\tilde{U}^m & -k^2\tilde{U}^m \end{bmatrix}, \end{aligned} \tag{17}$$

where $\tilde{U}^m$, $\tilde{\mathbf{b}}$, and $\tilde{\mathbf{T}}_\mathbf{m}$ represent the magnetic potential, field, and its gradient tensor in the mixed domain, respectively, and C is the same as equation 13. Partial derivatives and $\partial\tilde{U}^m/\partial z$ can be calculated via the partial-derivative method based on a quadratic shape function of the finite-element method (Xu, 1994), when the observation sites are located inside the sources.

Zero wavenumber processing

In particular, for a zero lateral wavenumber, the ordinary differential equations 4 and 6 that governs magnetic potential simplify to

$$\frac{\partial^2\tilde{U}^m(0,0,z)}{\partial z^2} = \frac{\partial\tilde{M}_z(0,0,z)}{\partial z}. \tag{18}$$

This is equivalent to the magnetic induction generated by a horizontally layered model regarding magnetization. The magnetic induction components can be written as

$$\tilde{b}_x(0,0,z) = 0, \tag{19}$$

$$\tilde{b}_y(0,0,z) = 0, \tag{20}$$

$$\tilde{b}_z(0,0,z) = \tilde{M}_z(0,0,z). \tag{21}$$

When the wavenumbers are equal to zero, ordinary differential equations 4 and 5 that govern gravitational potential can be simplified as

$$\frac{\partial^2\tilde{U}^g(0,0,z)}{\partial z^2} = -4\pi G\tilde{\rho}(0,0,z). \tag{22}$$

It is equivalent to the gravity fields generated by a horizontally layered model regarding to density. The three components of gravity field can be written as

$$\tilde{g}_x(0,0,z) = 0, \tag{23}$$

$$\tilde{g}_y(0,0,z) = 0, \tag{24}$$

$$\tilde{g}_z(0,0,z) = -4\pi G\int_{z_{\min}}^{z_{\max}} \text{sign}(z-z')\tilde{\rho}dz', \tag{25}$$

where $\text{sign}(z-z')$ is the same sign function as C in equation 13.

Solution of differential equations

The finite-element method based on a quadratic shape function is applied to solve 1D ordinary differential equation 4. The vertical grids can be arbitrarily adjusted with actual requirements, for example, fine grids at a shallow depth to approach complex topography and coarse grids at a deep depth to reduce the number of grids without unacceptably reducing the accuracy of the solution. Therefore, the calculation accuracy and efficiency of modeling can be relatively guaranteed simultaneously. The efficiency can be further improved by using a chasing method to solve the linear equation system with a fixed bandwidth (Temperton, 1975; Boisvert, 1991).

The boundary value problem of the gravity and magnetic potential in the mixed space-wavenumber domain can be described as

$$\begin{cases} \frac{\partial^2\tilde{U}(k_x,k_y,z)}{\partial z^2} - k^2\tilde{U}(k_x,k_y,z) = \tilde{f}(k_x,k_y,z), \\ \left.\frac{\partial\tilde{U}}{\partial z}\right|_{z=z_{\min}} = k\tilde{U}, \\ \left.\frac{\partial\tilde{U}}{\partial z}\right|_{z=z_{\max}} = -k\tilde{U}. \end{cases} \tag{26}$$

Based on the variational principle (Xu, 1994; Jin, 2014), the equivalence of a variational problem to the boundary value problem shown in equation 26 can be derived as

$$\begin{cases} F(\tilde{U}) = \int_{z_{\min}}^{z_{\max}}\left[\left(\frac{\partial\tilde{U}}{\partial z}\right)^2 + (k\tilde{U})^2 + 2\tilde{f}\,\tilde{U}\right]dz + k[(\tilde{U})^2_{z_{\max}} + (\tilde{U})^2_{z_{\min}}], \\ \delta F(\tilde{U}) = 0. \end{cases} \tag{27}$$

In the Cartesian coordinate system (Figure 1), we have a spatial cell along the z-direction, and the quadratic shape function is used in each cell. As a result, the potential, magnetization, and residual density change twice in each cell. We can finally assemble a full matrix by finite-element analysis cell by cell to obtain the following equation (see detailed derivations in Appendix A)

$$F(\tilde{U}) = \mathbf{u}^T\mathbf{K}\mathbf{u} - 2\mathbf{u}^T\mathbf{p}, \tag{28}$$

where $\mathbf{u}$ is a column vector of potential for each node in the z-direction and T denotes the transposition of a matrix. The terms $\mathbf{K}$ and $\mathbf{p}$ can be written as $\mathbf{K} = \sum \mathbf{K}_{1e} + \sum \mathbf{K}_{2e} + \mathbf{B}_1 + \mathbf{B}_2$ and $\mathbf{p} = \sum(-\mathbf{p}_{1e}\mathbf{sx}_e - \mathbf{p}_{2e}\mathbf{sy}_e - \mathbf{p}_{3e}\mathbf{sz}_e)$, respectively. The detailed expressions of $\mathbf{K}_{1e}$, $\mathbf{K}_{2e}$, $\mathbf{B}_1$, $\mathbf{B}_2$, $\mathbf{p}_{1e}$, $\mathbf{p}_{2e}$, $\mathbf{p}_{3e}$, $\mathbf{sx}_e$, $\mathbf{sy}_e$, and $\mathbf{sz}_e$ are shown in Appendix A. Using the variational principle on equation 28, we obtain

$$\delta F(\tilde{U}) = \delta\mathbf{u}^T(2\mathbf{K}\mathbf{u} - 2\mathbf{p}) = 0. \tag{29}$$

Due to the arbitrary nature of $\delta\mathbf{u}^T$, equation 29 can be simplified as

$$\mathbf{K}_{\mathrm{nz}\times 5}\mathbf{u}_{\mathrm{nz}} = \mathbf{p}_{nz}, \tag{30}$$

where $\mathbf{K}$ is a five-diagonal matrix, $\mathbf{p}$ is a column vector, and nz is the number of vertical nodes. The chasing method can achieve an efficient and accurate solution for the linear system shown in equation 30. After equation 30 is solved, it is straightforward to obtain the gravity and magnetic fields and their gradient tensors in the mixed domain by equations 12–13 and 16–17. Note that, at a certain combination of k_x and k_y, equation 30 is a small-scale problem, which needs much less computation and memory than solving the problem directly in 3D spatial domain. Regarding to different group of k_x and k_y, parallel computation can also be implemented. The selection of k_x and k_y can refer to Wu and Tian (2014). At the last step, we calculate the potential, fields, and gradient tensors in the spatial domain by inverse Fourier transform using standard FFT (Tontini et al., 2009) and Gauss FFT (Wu and Tian, 2014) methods.

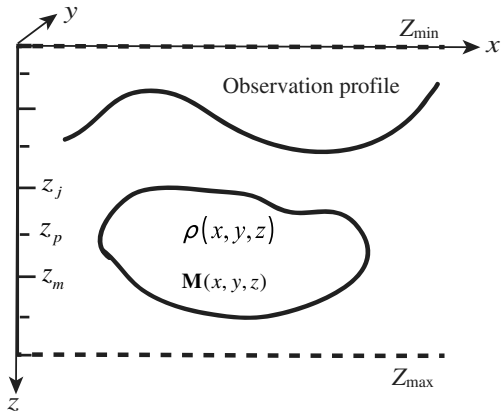

Figure 1. The anomaly model of density or magnetization. The upper and lower boundaries $Z_{\min}$ and $Z_{\max}$ for modeling are marked; x, y, and z are the directions of the Cartesian coordinate system; and z_j, z_p, and z_m are the values used for quadratic interpolation in finite element along the z-direction.

RESULTS

Synthetic model

A model composed of five prisms in Figure 2 is used for numerical experiments to achieve three goals: (1) verify the accuracy and efficiency of the proposed 3D numerical algorithm in the mixed space-wavenumber domain, (2) analyze the influences of grid expansion when using standard FFT method, and (3) compare the accuracy and computational costs between standard FFT method with grid expansion and the Gauss FFT method.

The modeling region is approximately $60 \times 60 \times 10\,\mathrm{km}^3$. It is divided into $202 \times 202 \times 101$ nodes resulting in the volume of each cell being $0.3 \times 0.3 \times 0.1\,\mathrm{km}^3$. One prism anomaly is located at the center of the model, and four smaller anomalies are symmetric based on the x- and y-directions. The volume of the central anomaly is $9 \times 9 \times 3\,\mathrm{km}^3$, and that of the smaller ones is $6 \times 6 \times 3\,\mathrm{km}^3$. The top of all the anomalies is at a 1.5 km depth.

For the magnetization anomalies, the magnetization rate of the anomalies χ is 0.01, the inclination angle is 45°, the declination angle is 0°, and the normal magnetic field of the earth is set as 50,000 nT. The residual density ρ is 2000 $\mathrm{kg/m}^3$.

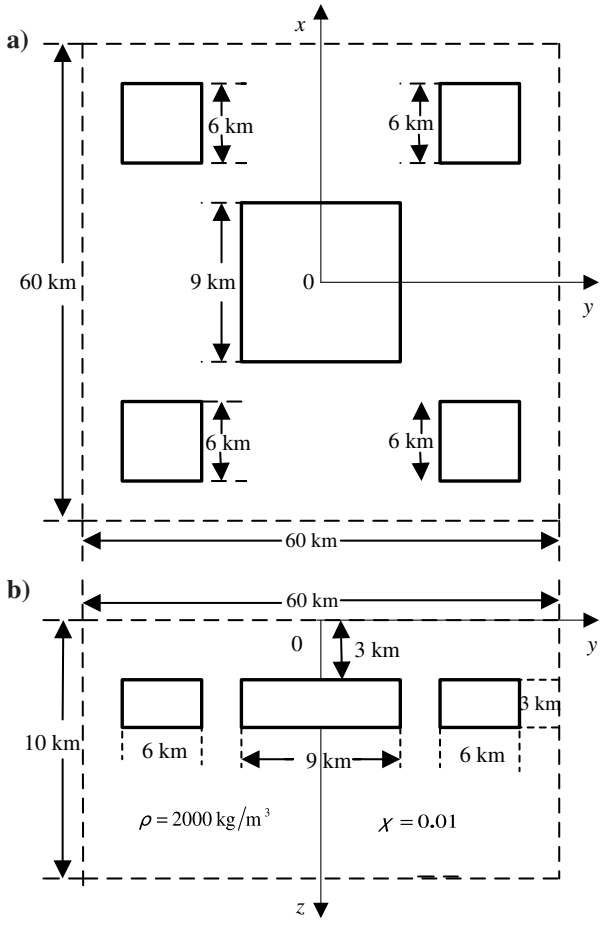

Figure 2. Synthetic model, either a density model or a magnetization model. (a) A horizontal slice of the model at $z = 0$ km depth and (b) the profile section along $x = 0$ km.

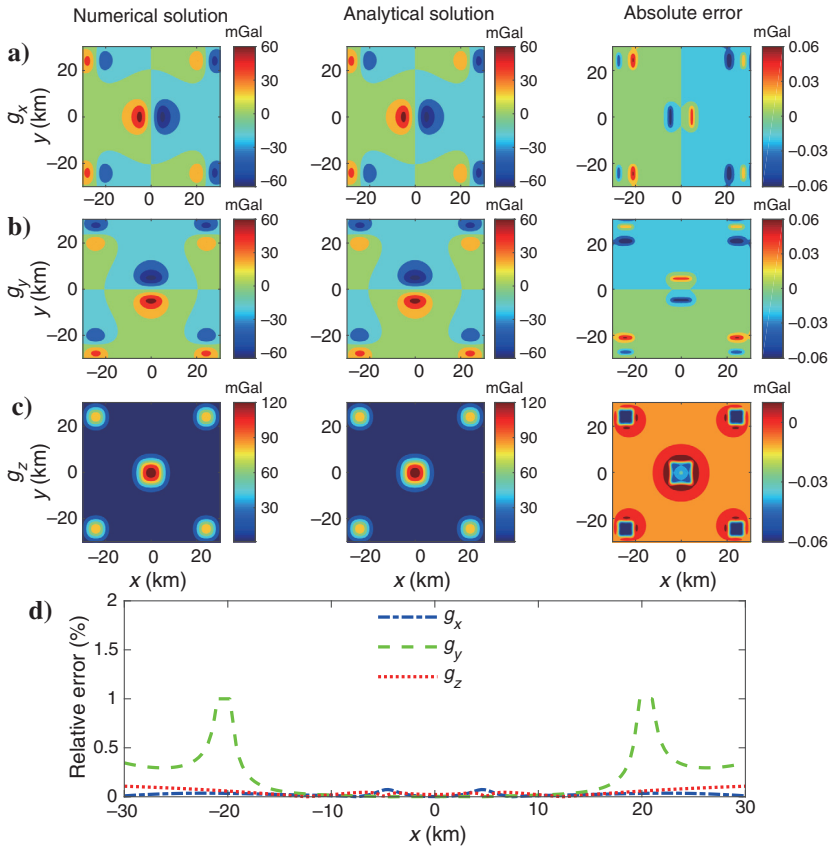

Figure 3. Numerical solution, analytical solution, and the error of the gravity fields, (a) g_x, (b) g_y, and (c) g_z, on the plane of $z = 0$ km. High values of g_x and g_y are caused by the side boundaries of the anomalies, and high values of g_z are caused by the top and bottom boundaries of the anomalies. Errors mainly exist at the positions corresponding to the locations of anomalies. (d) Relative errors of gravity fields along the profile of $z = 0$ km and $y = 0.3$ km. The relatively large relative errors caused by the boundaries of the central anomaly in the model, and the maximum relative error of g_y at the cusp is truncated to 1% to show better error visualization, and the reason is that at cusp positions, the field values are extremely small and very hard to get an accurate solution.

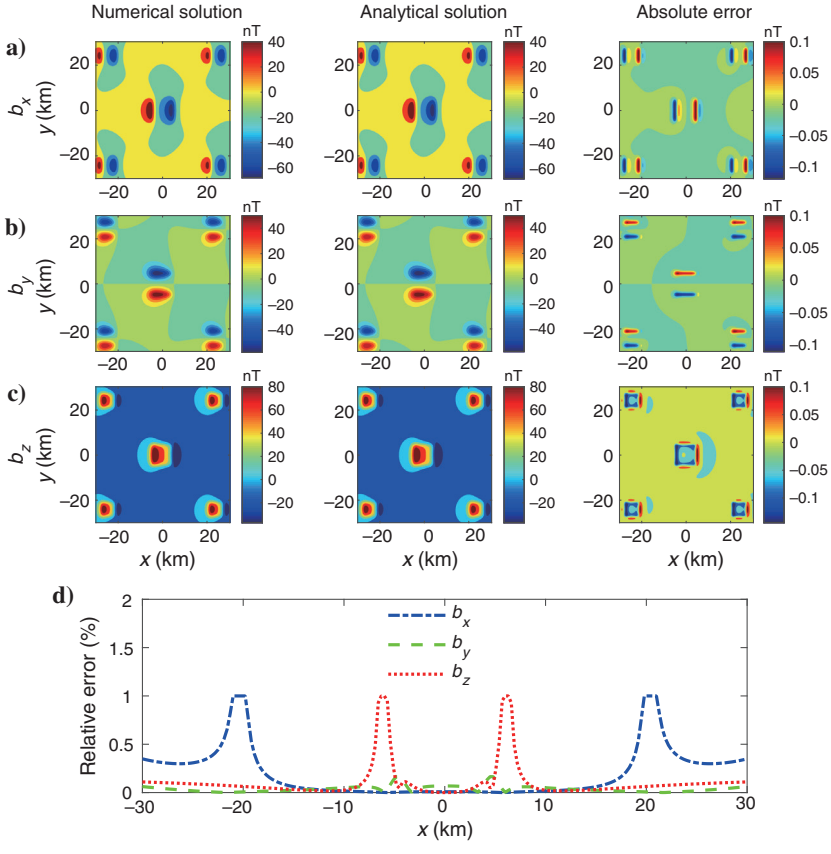

Figure 4. Numerical solution, analytical solution, and the error of magnetic fields, (a) b_x, (b) b_y, and (c) b_z, on the plane of $x = 0$ km. High values of b_x and b_y are caused by the side boundaries of the anomalies, and high values of b_z are caused by the top and bottom boundaries of the anomalies. Errors mainly exist at the positions corresponding to the locations of anomalies. (d) Relative errors of magnetic fields along the profile of $z = 0$ km and $y = 0.3$ km. The relatively large relative errors caused by the boundaries of the central anomaly in the model, and the maximum relative error of b_y at the cusp is also truncated to 1% to show better error visualization.

Algorithm accuracy and efficiency

To verify the accuracy and efficiency of the new 3D numerical modeling method for gravity and magnetic anomaly in the mixed space-wavenumber domain, the Gauss-FFT based on four values of Gaussian points is used in the proposed algorithm due to its high-precision characteristics (Wu and Tian, 2014). The closed-form solutions (such as Blakely, 1996; Li and Chouteau, 1998; Heath et al., 2005) of the gravity and magnetic fields, gradient tensors for these simple prismatic bodies (Figure 2) are used to show the accuracy of the proposed method.

Three components of gravity and magnetic anomaly fields in Figures 3 and 4 show that the fields are sensitive to the boundaries of anomalies. The maximum absolute errors of the gravity and magnetic anomaly fields are 0.06 mGal and 0.1 nT (Figures 3a–3c and 4a–4c), respectively. The relative errors of gravity and magnetic fields along the profile of $z = 0$ km and $y = 0.3$ km are smaller than one percent except at the corresponding positions of the anomaly boundaries (Figures 3d and 4d). One clear indication is that the relatively large errors, especially for g_z, b_y, and b_z, are caused by the strong contrast of anomalies at either the side boundaries or the top and bottom boundaries.

Nine components of gravity and magnetic tensors in Figures 5 and 6 show that the gravity and magnetic gradient tensors are sensitive to either the boundaries or the corners of anomalies. The maximum absolute errors of the gravity and magnetic tensors are 0.6Eotvos(E) and 2×10^{-4} nT/m (Figures 5 and 6), respectively. The large modeling errors mostly exist due to the strong contrast at the positions of anomaly boundaries in the model. However, the T_{xy} components of the gravity and magnetic gradient tensor show that the large values may be caused by the corners of the anomalies rather than the boundaries. Generally, the accuracy and reliability of the proposed algorithm are high enough to study the potential fields or for inverse imaging. If a finer mesh is used at a price of increased computation, the absolute errors of the gravity field and gradient tensors could be further reduced.

The proposed method is compared with the method presented by Tontini et al. (2009) using the standard FFT and Gauss-FFT (four Gaussian points) for the same model as in Figure 2. The code of Zhao et al. (2018) is selected to do the comparison, because the code has implemented Tontini's method with the standard FFT and Gauss-FFT and is also available. The machine used has four processors of 3.3 GHz Intel Core i5 and 16 GB memory in total. The time comparisons of our approach to Tontini's approach with different numbers of observational surfaces are shown in Table 1. Tontini's method with 3D FFT is more efficient than the proposed method with 2D FFT when standard FFT method is used. However, the proposed method is more efficient than Tontini's method when the Gauss-FFT method is used (Table 1), which has better accuracy than standard FFT. Thus, the proposed method is more efficient and suitable for modeling with the Gauss-FFT method.

Balance between accuracy and efficiency

Accuracy and computational efficiency are two important indicators for the quality of numerical modeling. Wu and Tian (2014) introduce the Gauss FFT method reducing the influence of the truncated boundary effect to improve the accuracy of the numerical modeling. This method, though, increases the computation time. To account for the accuracy and computational cost, we studied the accuracy and efficiency of the numerical modeling using the standard FFT method with grid expansion and the Gauss FFT method.

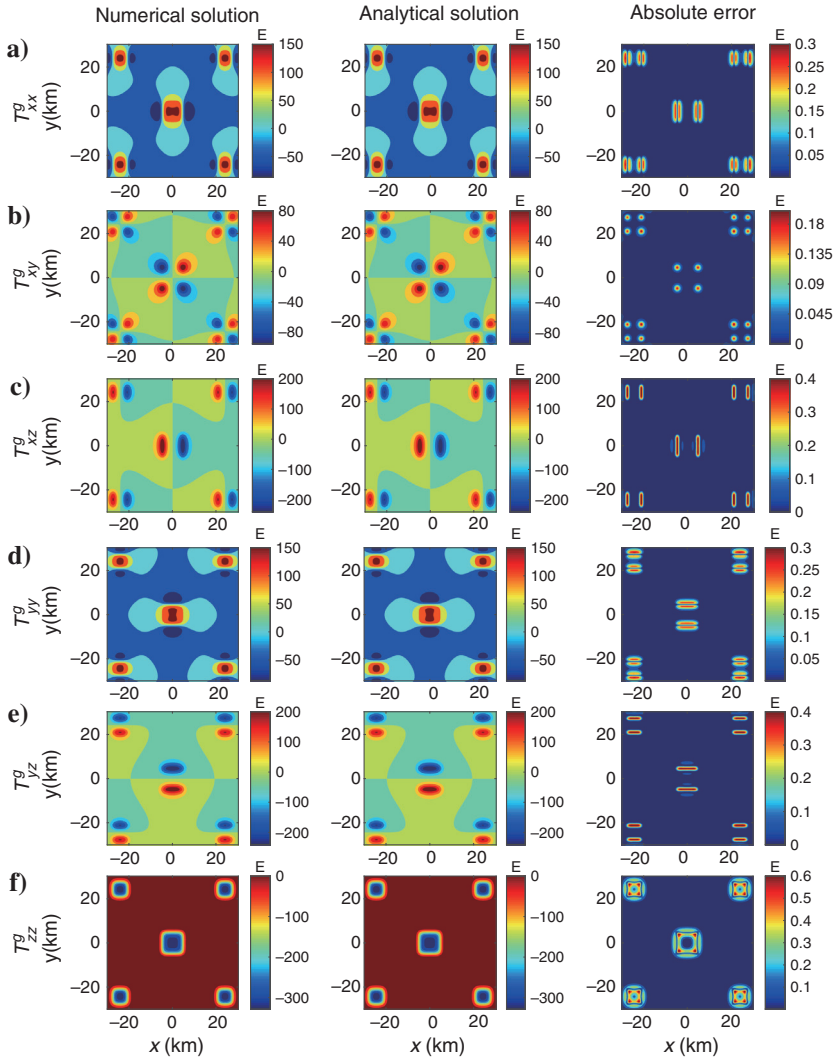

Figure 5. Numerical solution, analytical solution, and absolute errors of gravity gradient tensor, (a) T_{xx} component, (b) T_{xy} component, (c) T_{xz} component, (d) T_{yy} component, (e) T_{yz} component, and (f) T_{zz} component, on the plane of $z = 0$ km. It seems T_{xy} component of gravity gradient tensor contains information of the corners of anomalies. All other shown components of gravity gradient tensor contain different information of the boundaries of the anomalies. Errors mainly exist at the positions corresponding to the locations of the boundaries of the anomalies.

First, the relationship between the expansion distance and the depth of the anomaly as well as other influences on the accuracy of the algorithm are analyzed.

The expansion coefficient K_e, an important indicator to measure the extent of expansion, is defined as

$$K_e = \frac{K_b}{D}, \tag{31}$$

where K_b is the expansion distance, D is the depth to the anomaly center, and K_e reflects the ratio of K_b to D.

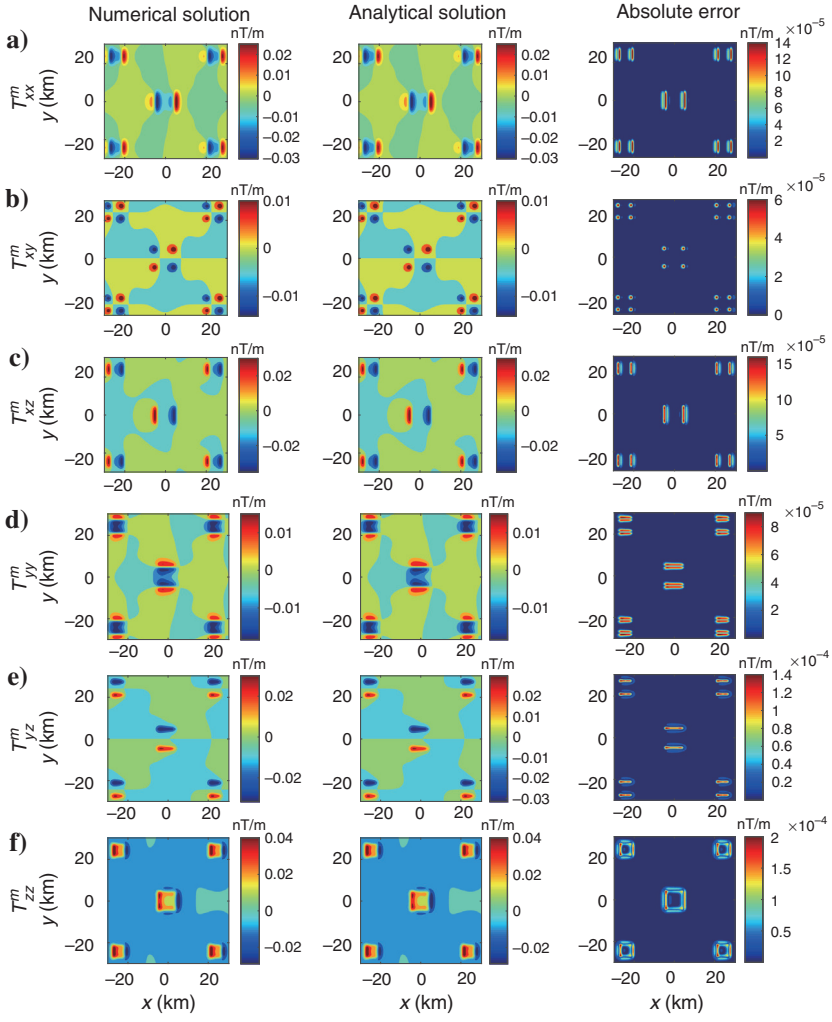

Figure 6. Numerical solution, analytical solution, and absolute errors of magnetic gradient tensor, (a) T_{xx} component, (b) T_{xy} component, (c) T_{xz} component, (d) T_{yy} component, (e) T_{yz} component, and (f) T_{zz} component, on the plane of $z = 0$ km. The general features of magnetic gradient tensor are similar to the ones of gravity gradient tensor in Figure 5.

Table 1. Comparison of computational time between Tontini's method (Tontini et al., 2009) and our proposed method for modeling the vertical component of the gravity field. The model used is shown in Figure 2. The total number of elements Q is 4,040,100. The observation sites are set as 201×201 and $201 \times 201 \times 101$ for one observational surface and 101 observational surfaces, respectively, in Tontini's method. Tontini's method sets each element as a parameter, and the proposed method sets each node as a parameter so that the total observation sites are 202×202 and $202 \times 202 \times 101$ in our method. The small difference of parameterization of the two methods cannot cause an obvious difference of calculation time.

Q	Observations	Time (s)			
		Tontini's method with 3D FFT	Proposed method with 2D FFT	Tontini's method with 3D Gauss-FFT	Proposed method with 2D Gauss-FFT
4,040,100	40,401	0.6	1.4	81.4	18.9
	4,040,100	0.6	2.1	81.4	27.8

The formula of the relative root-mean-square (Rrms) error (Wu, 2016) shown in equation 32 is used to study the accuracy of the standard FFT method with grid expansion and the Gauss FFT method for the modeling:

$$\text{Rrms} = \frac{\sqrt{\sum_{i=1}^{M}\sum_{j=1}^{L}(H_{ij}-\hat{H}_{ij})^2}}{\sqrt{\sum_{i=1}^{M}\sum_{j=1}^{L}\hat{H}_{ij}^2}} \times 100\%, \qquad (32)$$

where M and L are the numbers of observation points in the x- and y-directions, respectively, and H_{ij} and $\hat{H}_{ij}$ represent the numerical solution and analytic solution, respectively. The Rrms normalizes the absolute errors to the same error level no matter how large or small the gravity or magnetic fields and their gradients are.

Table 2 shows that the Rrms of the gravity fields calculated by the standard FFT method are relatively large when the expansion coefficient K_e is less than 10, but it decreases with the increase of the expansion coefficient. When the expansion coefficient is no less than 10, the Rrms of the gravity gradient tensors is less than 1%, whereas the Rrms of the horizontal components of the gravity fields is relatively large. The accuracy of the proposed algorithm meets the practical requirements when the expansion coefficient is no less than 10 based on the study. Thus, the modeling code can be used for inversion implementation in further study.

Table 2 also shows that the Rrms of using the Gauss FFT method based on two Gaussian points is large. The Gauss FFT method based on four Gaussian points can effectively suppress the boundary truncation effect and obtain high accuracy, but at the expense of greater computation cost. When the expansion coefficient is 10 for the standard FFT method, the agreement between the numerical solution and the analytical solution of the gravity fields in the observation zone are decent and the Rrms is less than 1% (Figure 7). Although the numerical accuracy of the Gauss FFT method based on four Gauss points is not reached by the standard FFT method, with the expansion coefficient of 10 or 15, the standard FFT method is able to maintain a reasonable balance between accuracy and computational efficiency and satisfies the requirements for practical applications.

Table 3 shows that the Rrms of the magnetic fields are relatively large when the expansion coefficient is less than 10, but it decreases obviously with the increase of the expansion coefficient. When the expansion coefficient is no less than 10, the Rrms of the magnetic field and the magnetic tensor become smaller, and then the Rrms is almost constant as the expansion coefficient increasing. Also, when the expansion coefficient is 10, the numerical solution, by the standard FFT method, and the analytical solution of the magnetic fields match well in the observation area as shown in Figure 8.

To study the modeling efficiency of the standard FFT method with the grid extension and Gauss FFT methods, the calculation time for 1 observational surface and 101 observational surfaces of the gravity/magnetic fields is compared. The comparisons between computational time are based on different expansion coefficients and different Gaussian points.

A comparison of the calculation time obtained with different Fourier transform methods based on the given model (Figure 2) is shown in Figure 9. Sequential computation and parallel computation are used in the comparison. When the expansion coefficient is

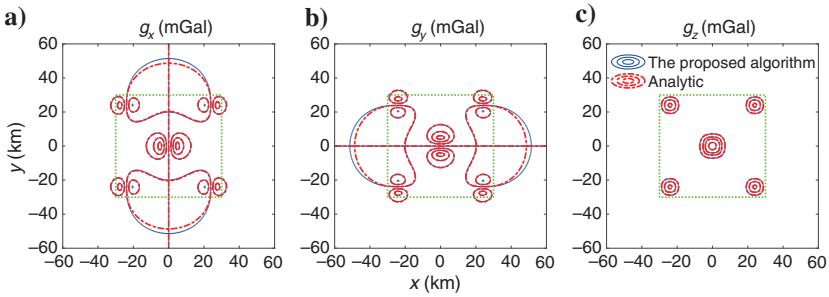

Figure 7. The numerical and analytical solutions of the gravity fields at the earth's surface with the expansion coefficient of 10, (a) g_x component, (b) g_y component, and (c) g_z component. The dotted green line marks the observation area.

Table 2. Rrms of the gravity field and gravity gradient tensors at the surface ($z = 0$) in percent, where K_e is the expansion coefficient and N is the number of Gaussian points.

	Standard FFT method with grid expansion					Gauss FFT method	
Mesh generation	244×244	304×304	406×406	508×508	610×610	202×202	202×202
K_e or N	$K_e = 2$	$K_e = 5$	$K_e = 10$	$K_e = 15$	$K_e = 20$	$N = 2$	$N = 4$
g_x	17.4972	7.5090	2.8795	1.4252	0.8114	7.1635	0.0668
g_y	17.4972	7.5090	2.8795	1.4252	0.8114	7.1635	0.0668
g_z	5.2854	2.4040	1.0168	0.5519	0.3436	3.3666	0.0477
T^g_{xx}	4.6153	1.8886	0.7106	0.3640	0.2331	4.2048	0.1389
T^g_{xy}	1.9170	0.4169	0.1946	0.1214	0.1088	7.4030	0.1020
T^g_{xz}	0.6129	0.1504	0.1255	0.1251	0.1251	2.9833	0.1248
T^g_{yy}	4.6153	1.8886	0.7106	0.3640	0.2331	4.2048	0.1389
T^g_{yz}	0.6129	0.1504	0.1255	0.1251	0.1251	2.9833	0.1248
T^g_{zz}	5.3608	2.2235	0.8442	0.4400	0.2893	2.8806	0.1811

10 (Tables 2 and 3) and the mesh size is $406 \times 406 \times 101$, the sequential computation time of 1 observational surface with 202×202 data points is 6.6 s (the fifth green circle) and the calculation time of 101 observational surfaces with $202 \times 202 \times 101$ data points is 16.8 s (the fifth blue triangle). The difference of the parallel computation for 202×202 data points and $202 \times 202 \times 101$ data points on the same mesh (the difference between the fifth red star and the fifth purple diamond) is smaller than the one of the sequential computation time (the difference between the fifth green circle and the fifth blue triangle). Even though the calculation accuracy of the Gauss FFT method based on four Gaussian points is higher than the standard FFT method with grid extension (Tables 2 and 3), the runtime of the Gauss FFT method with four Gaussian points, is more than the standard FFT method regarding the meshes smaller than the mesh of $610 \times 610 \times 101$ (Figure 9). However, when the mesh used for standard FFT with grid extension is $610 \times 610 \times 101$, the Gauss FFT method shows advantages in efficiency and accuracy. Interestingly, the runtime difference between modeling of one observational surface and of 100 observational surfaces is about two to three times no matter which method was used and whether parallelization was used. Because the method solves the equations once to obtain the potential, fields, gradient tensors for all the observation sites, the increased time for multiple observational surfaces is mainly spent on the fast 2D Fourier transforms.

Anomaly with a fluctuated observational surface

The second synthetic model is an anomaly in half-space homogeneous media with topography (Figure 10). The minimum and maximum observational heights are 0.038 and 0.624 km, respectively. The size of the model is $10 \times 10 \times 1.324$ km. An anomalous density of 2000 kg/m^3 is assigned to the anomaly. The size of the anomaly is $2 \times 2 \times 0.3$ km, and its center is 0.55 km below the 0 km depth. The structured mesh used has $201 \times 201 \times 101$ source nodes, and 201×201 observation sites are distributed on a fluctuated surface that in fact was composed by 31 flat surfaces uniformly spaced in the z-direction. This model demonstrates the ability of our method to model the gravity anomaly with topography. The gravity fields on the fluctuated surface are calculated by our proposed modeling approach with cubic spline interpolation and the closed-form solution (Blakely, 1996; Li and Chouteau, 1998). Using four processors on the machine, the calculation took 25.3 s. The comparisons for the gravity fields are presented in Figure 11. The maximal relative error of g_x, g_y, and g_z is no larger than 0.3%. So that the proposed method shows good numerical

Table 3. Rrms of the magnetic field and magnetic gradient tensors at the surface area in percent, where K_e is the expansion coefficient and N is the number of Gaussian points.

	Standard FFT method with grid expansion					Gauss FFT method	
Mesh size	244×244	304×304	406×406	508×508	610×610	202×202	202×202
$K_e$or N	$K_e = 2$	$K_e = 5$	$K_e = 10$	$K_e = 15$	$K_e = 20$	$N = 2$	$N = 4$
b_x	1.0087	0.2275	0.1416	0.1244	0.1222	4.2634	0.1207
b_y	3.0334	1.2280	0.4697	0.2542	0.1786	3.6880	0.1311
b_z	4.3885	1.8159	0.6855	0.3510	0.2230	2.8530	0.1253
T^m_{xx}	0.5761	0.3650	0.3624	0.3623	0.3622	3.7576	0.3636
T^m_{xy}	0.6829	0.2410	0.2338	0.2333	0.2332	4.6531	0.2331
T^m_{xz}	0.4995	0.3322	0.3271	0.3269	0.3269	1.6669	0.3269
T^m_{yy}	0.6843	0.3960	0.3871	0.3867	0.3866	3.1021	0.3877
T^m_{yz}	0.4960	0.3633	0.3596	0.3595	0.3595	2.2157	0.3603
T^m_{zz}	0.4653	0.3491	0.3464	0.3464	0.3463	2.1301	0.3470

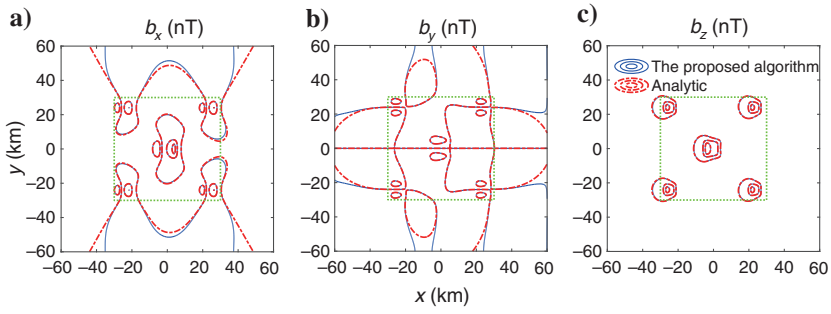

Figure 8. The numerical solution and analytical solution of the magnetic fields at the earth's surface with the expansion coefficient of 10, (a) b_x component, (b) b_y component, and (c) b_z component. The dotted green line marks the observation area.

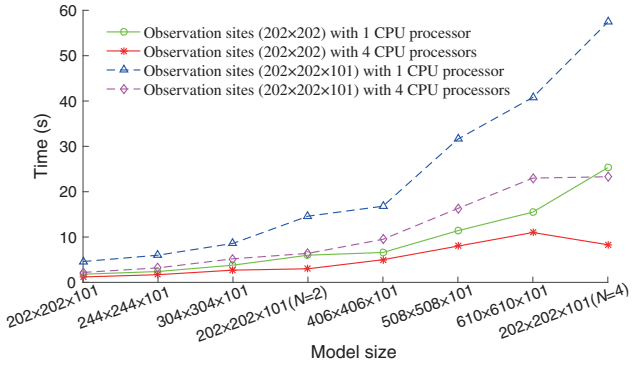

Figure 9. The comparison of the calculation time obtained with different Fourier transformation methods. The time is for calculating the magnetic potential and fields of a given 3D model parameterization. The value N is the number of Gaussian points. These models marked with $202 \times 202 \times 101$ ($N = 2$) and $202 \times 202 \times 101$ ($N = 4$) mean that two Gaussian points and four Gaussian points were used to calculate observations at 101 surfaces with a grid size of 202×202, respectively. A 2D FFT with grid expansion was used to calculate observations for all other models.

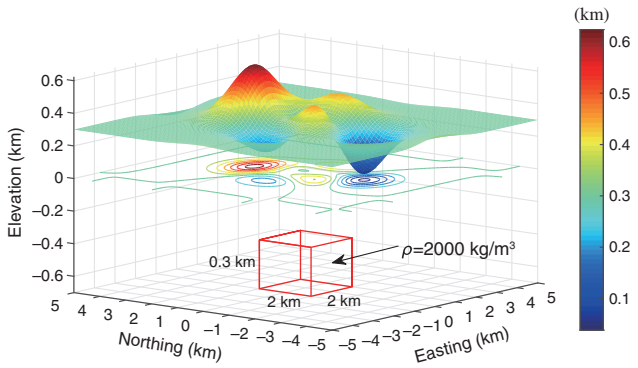

Figure 10. An anomaly in a homogeneous half-space with topography, and the terrain contours are projected at the surface of $z = 0$ km. The anomaly is the red outlined cube, and it has a density of 2000 kg/m^3. The volume of the anomaly is $2 \times 2 \times 0.3$ km, and its center is 0.55 km below the 0 km depth. With topography, the anomalous responses can still be captured.

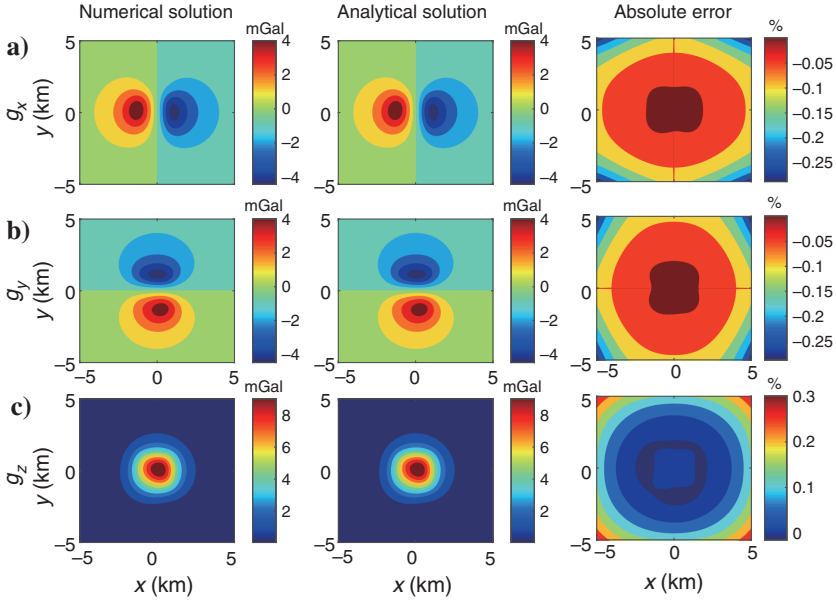

Figure 11. Numerical solution, analytical solution, and the relative errors of the gravity fields, (a) g_x, (b) g_y, and (c) g_z, on a fluctuated observational surface. The numerical solution is obtained by our approach. The analytical solution is the closed-form solution. Calculation of the relative error is based on equation 32.

accuracy for the modeling of topography and is suitable for field-data application in the future.

CONCLUSION

An efficient and accurate 3D numerical modeling of gravity and magnetic anomaly in the mixed space-wavenumber domain is proposed and implemented in this study. This method transforms the 3D PDE in the spatial domain into a 1D ordinary differential equation using the 2D Fourier transform along the horizontal directions so that the memory requirement is greatly reduced. The method preserves the vertical component in the spatial domain; thus, the mesh for modeling can be fine at the shallow depth and coarse at the deep depth. This, to some extent, is an advantage for the modeling with complex topography. Generally, this method takes into account the modeling accuracy and the calculation efficiency. The finite-element method is used to solve the ordinary differential equations containing different wavenumbers, and the efficiency of solving the linear equations with a fixed bandwidth is further improved by the chasing method.

In the numerical experiments, a model with five prism anomalies and a simple model with topography were used to verify the accuracy, efficiency, and potential ability of the proposed algorithm. In addition, we also compared the calculation accuracy and efficiency of the standard FFT method with grid expansion and the Gaussian FFT method. The results of the comparisons show that the standard FFT method with grid expansion and the Gauss-FFT method have their own advantages in efficiency and accuracy, respectively. The implementation of parallelization over independent wavenumbers dramatically reduces the computation time. Even though the

proposed method using standard FFT is slower than Tontini's method, the proposed method using Gauss FFT is twice as fast as Tontini's method. The proposed method can maintain a desired balance between accuracy and efficiency. These findings will benefit inversion and quantified interpretation in our future work.

ACKNOWLEDGMENTS

This study was supported by the Natural Science Foundation of China (grant no. 41574127), the National Science and Technology Major Project of China (grant no. 2017YFC0602204-10), the China Postdoctoral Science Foundation (grant no. 2017M622608), and the project for the independent exploration of graduate students at Central South University (grant no. 2017zzts008). S. Wang thanks the Seafloor Electromagnetic Methods Consortium and Green Foundation at Scripps Institution of Oceanography for supporting his postdoctoral research. The editors, Y. Li and J. Shragge, and Z. Ren and three anonymous reviewers are appreciated for the constructive comments that improved our manuscript.

DATA AND MATERIALS AVAILABILITY

Data associated with this research are available and can be obtained by contacting the corresponding author.

APPENDIX A

FINITE-ELEMENT ANALYSIS

The integral of the whole modeling region is decomposed into the sum of the integral of each element, then equation 27 can be reformed as

$$F(\tilde{U}) = \sum \int_e \left(\frac{\partial \tilde{U}}{\partial z}\right)^2 dz + \sum \int_e (k\tilde{U})^2 dz + 2\sum \int_e \tilde{f}\,\tilde{U}\,dz + k(\tilde{U})^2_{z_{\min}} + k(\tilde{U})^2_{z_{\max}}. \quad \text{(A-1)}$$

Based on finite-element theory, we define quadratic shape function and potential values at the nodes as

$$\left.\begin{aligned} \mathbf{N} &= (N_j, N_p, N_q)^T \\ \mathbf{u}_e &= (\tilde{U}_j, \tilde{U}_p, \tilde{U}_q)^T \end{aligned}\right\}. \quad \text{(A-2)}$$

Then, the values at arbitrary position can be written as

$$u = \mathbf{N}^T\mathbf{u}_e = \mathbf{u}_e^T\mathbf{N}. \quad \text{(A-3)}$$

The first-element integral in equation A-1 is

$$\int_e \left(\frac{\partial \tilde{U}}{\partial z}\right)\left(\frac{\partial \tilde{U}}{\partial z}\right) dz = \mathbf{u}_e^T\left[\int_e \left(\frac{\partial \mathbf{N}}{\partial z}\frac{\partial \mathbf{N}^T}{\partial z}\right) dz\right]\mathbf{u}_e = \mathbf{u}_e^T\mathbf{K}_{1e}\mathbf{u}_e, \quad \text{(A-4)}$$

where

$$\mathbf{K}_{1e} = \int_e \left(\frac{\partial \mathbf{N}}{\partial z}\frac{\partial \mathbf{N}^T}{\partial z}\right) dz = \frac{1}{3l}\begin{pmatrix} 7 & -8 & 1 \\ -8 & 16 & -8 \\ 1 & -8 & 7 \end{pmatrix}. \quad \text{(A-5)}$$

The second-element integral in equation A-1 is

$$\int_e (k\tilde{U})^2 \mathrm{dz} = \mathbf{u}_e^T\left(\int_e k^2\mathbf{N}\mathbf{N}^T \mathrm{dz}\right)\mathbf{u}_e = \mathbf{u}_e^T\mathbf{K}_{2e}\mathbf{u}_e, \quad \text{(A-6)}$$

where

$$\mathbf{K}_{2e} = \int_e k^2\mathbf{N}\mathbf{N}^T \mathrm{dz} = \frac{lk^2}{30}\begin{pmatrix} 4 & 2 & -1 \\ 2 & 16 & 2 \\ -1 & 2 & 4 \end{pmatrix}. \quad \text{(A-7)}$$

And, the third-element integral in equation A-1 is

$$\int_e 2\tilde{f}\,\tilde{U}\,dz = \int_e 2ik_x j_{ax}\tilde{U}dz + \int_e 2ik_y j_{ay}\tilde{U}dz + \int_e 2\frac{\partial j_{az}}{\partial z}\tilde{U}dz. \quad \text{(A-8)}$$

Here, j_{ax}, j_{ay}, and j_{az} are shown as

$$\left.\begin{aligned} j_{ax} &= j_{axj}N_j + j_{axp}N_p + j_{axm}N_m = \mathbf{N}^T\mathbf{sx}_e = \mathbf{sx}_e^T\mathbf{N} \\ j_{ay} &= j_{ayj}N_j + j_{ayp}N_p + j_{aym}N_m = \mathbf{N}^T\mathbf{sy}_e = \mathbf{sy}_e^T\mathbf{N} \\ j_{az} &= j_{azj}N_j + j_{azp}N_p + j_{aym}N_m = \mathbf{N}^T\mathbf{sz}_e = \mathbf{sz}_e^T\mathbf{N} \end{aligned}\right\}, \quad \text{(A-9)}$$

where $\mathbf{sx}_e$, $\mathbf{sy}_e$, and $\mathbf{sz}_e$ are

$$\left.\begin{aligned} \mathbf{sx}_e &= (j_{axj}, j_{axp}, j_{axm})^T \\ \mathbf{sy}_e &= (j_{ayj}, j_{ayp}, j_{aym})^T \\ \mathbf{sz}_e &= (j_{azj}, j_{azp}, j_{azm})^T \end{aligned}\right\}. \quad \text{(A-10)}$$

The first-element integral in equation A-8 is

$$\int_e ik_x j_{ax}\tilde{U}dz = \mathbf{u}_e^T\left(\int_e ik_x\mathbf{N}\mathbf{N}^T dz\right)\mathbf{sx}_e = \mathbf{u}_e^T\mathbf{p}_{1e}\mathbf{sx}_e, \quad \text{(A-11)}$$

where

$$\mathbf{p}_{1e} = \int_e ik_x\mathbf{N}\mathbf{N}^T dz = \frac{ik_x l}{30}\begin{pmatrix} 4 & 2 & -1 \\ 2 & 16 & 2 \\ -1 & 2 & 4 \end{pmatrix}. \quad \text{(A-12)}$$

The second-element integral in equation A-8 is

$$\int_e ik_y j_{ay}\tilde{U}dz = \mathbf{u}_e^T\left(\int_e ik_y\mathbf{N}\mathbf{N}^T dz\right)\mathbf{sy}_e = \mathbf{u}_e^T\mathbf{p}_{2e}\mathbf{sy}_e, \quad \text{(A-13)}$$

where

$$\mathbf{p}_{2e} = \int_e ik_y \mathbf{N}\mathbf{N}^T dz = \frac{ik_y l}{30}\begin{pmatrix} 4 & 2 & -1 \\ 2 & 16 & 2 \\ -1 & 2 & 4 \end{pmatrix}. \quad \text{(A-14)}$$

The third-element integral in equation A-8 is

$$\int_e \frac{\partial j_{az}}{\partial z}\tilde{U}dz = \mathbf{u}_e^T\left(\int_e \frac{\partial \mathbf{N}}{\partial z}\mathbf{N}^T \mathrm{d}z\right)\mathbf{sz}_e = \mathbf{u}_e^T\mathbf{p}_{3e}\mathbf{sz}_e, \quad \text{(A-15)}$$

where

$$\mathbf{p}_{3e} = \int_e \frac{\partial \mathbf{N}}{\partial z}\mathbf{N}^T dz = \frac{1}{6}\begin{pmatrix} -3 & -4 & 1 \\ 4 & 0 & -4 \\ -1 & 4 & 3 \end{pmatrix}. \quad \text{(A-16)}$$

In equation A-1, $z = z_{\min}$ and $z = z_{\max}$ are the vertical coordinate at the first and last nodes, respectively, and the last two terms of equation A-1 can be reshaped into

$$k(\tilde{U})^2_{z_{\min}} = \mathbf{u}^T\mathbf{B}_1\mathbf{u}, \quad k(\tilde{U})^2_{z_{\max}} = \mathbf{u}^T\mathbf{B}_2\mathbf{u}\,, \quad \text{(A-17)}$$

where

$$\mathbf{B}_1 = \begin{pmatrix} k & \cdots & 0 \\ \cdots & \cdots & \cdots \\ 0 & \cdots & 0 \end{pmatrix}, \quad \mathbf{B}_2 = \begin{pmatrix} 0 & \cdots & 0 \\ \cdots & \cdots & \cdots \\ 0 & \cdots & k \end{pmatrix}. \quad \text{(A-18)}$$

Based on the above finite-element analysis, the final equation can be written as

$$F(\tilde{U}) = \mathbf{u}^T\mathbf{K}\mathbf{u} - 2\mathbf{u}^T\mathbf{p}. \quad \text{(A-19)}$$

REFERENCES

Aitken, A. R. A., M. L. Salmon, and B. L. N. Kennett, 2013, Australia's Moho: A test of the usefulness of gravity modeling for the determination of Moho depth: Tectonophysics, **609**, 468–479, doi: 10.1016/j.tecto.2012.06.049.

Barnett, C., 1976, Theoretical modeling of the magnetic and gravitational fields of an arbitrarily shaped three-dimensional body: Geophysics, **41**, 1353–1364, doi: 10.1190/1.1440685.

Bhattacharyya, B., 1964, Magnetic anomalies due to prism-shaped bodies with arbitrary polarization: Geophysics, **29**, 517–531, doi: 10.1190/1.1439386.

Bhattacharyya, B., 1966, Continuous spectrum of the total-magnetic-field anomaly due to a rectangular prismatic body: Geophysics, **31**, 97–121, doi: 10.1190/1.1439767.

Blakely, R. J., 1996, Potential theory in gravity and magnetic applications: Cambridge University Press.

Boisvert, R. F., 1991, Algorithms for special tridiagonal systems: Society for Industrial and Applied Mathematics, **12**, 423–442, doi: 10.1137/0912023.

Cai, Y., and C. Y. Wang, 2005, Fast finite-element calculation of gravity anomaly in complex geological regions: Geophysical Journal International, **162**, 696–708, doi: 10.1111/j.1365-246X.2005.02711.x.

Chai, Y., 1997, Shift sampling theory of Fourier transform computation: Science in China series E: Technological Sciences, **40**, 21–27, doi: 10.1007/BF02916587.

Chakravarthi, V., H. M. Raghuram, and S. B. Singh, 2002, 3-D forward gravity modeling of basement interfaces above which the density contrast varies continuously with depth: Computers and Geosciences, **28**, 53–57, doi: 10.1016/S0098-3004(01)00080-2.

Dutra, A. C., Y. R. Marangoni, and T. C. Junqueira-Brod, 2012, Investigation of the Goiás Alkaline Province, Central Brazil: Application of gravity and magnetic methods: Journal of South American Earth Sciences, **33**, 43–55, doi: 10.1016/j.jsames.2011.06.004.

Eppelbaum, L. V., 2011, Study of magnetic anomalies over archaeological targets in urban environments: Physics and Chemistry of the Earth, Parts A/B/C, **36**, 1318–1330, doi: 10.1016/j.pce.2011.02.005.

Farquharson, C. G., and C. R. W. Mosher, 2009, Three-dimensional modeling of gravity data using finite differences: Journal of Applied Geophysics, **68**, 417–422, doi: 10.1016/j.jappgeo.2009.03.007.

Feng, R., 1986, The potential field calculation of the three-dimensional physical distribution (in Chinese): Chinese Journal of Geophysics, **29**, 399–406.

Forsberg, R., 1985, Gravity field terrain effect computations by FFT: Bulletin Géodésique, **59**, 342–360, doi: 10.1007/BF02521068.

Furness, P., 1994, A physical approach to computing magnetic fields: Geophysical Prospecting, **42**, 405–416, doi: 10.1111/j.1365-2478.1994.tb00218.x.

García-Abdeslem, J., 2005, The gravitational attraction of a right rectangular prism with density varying with depth following a cubic polynomial: Geophysics, **70**, no. 6, J39–J42, doi: 10.1190/1.2122413.

Granser, H., 1987, Nonlinear inversion of gravity data using the Schmidt-Lichtenstein approach: Geophysics, **52**, 88–93, doi: 10.1190/1.1442243.

Guzman, S., 2015, Forward modeling and inversion of potential field data using partial differential equations: Ph.D. thesis, Colorado School of Mines.

Haber, E., E. Holtham, and K. Davis, 2014, Large-scale inversion of gravity gradiometry with differential equations: 84th Annual International Meeting, SEG, Expanded Abstracts, 1302–1307, doi: 10.1190/segam2014-1415.1.

Heath, P. J., S. Greenhalgh, and N. G. Direen, 2005, Modeling gravity and magnetic gradient tensor responses for exploration within the regolith: Exploration Geophysics, **36**, 357–364, doi: 10.1071/EG05357.

Holstein, H., 2002, Gravimagnetic similarity in anomaly formulas for uniform polyhedra: Geophysics, **67**, 1126–1133, doi: 10.1190/1.1500373.

Jahandari, H., and C. G. Farquharson, 2013, Forward modeling of gravity data using finite-volume and finite-element methods on unstructured grids: Geophysics, **78**, no. 1, G69–G80, doi: 10.1190/GEO2012-0246.1.

Jin, J. M., 2014, The finite element method in electromagnetics, 3rd ed.: Wiley-IEEE Press.

Kamm, J., I. A. Lundin, M. Bastani, M. Sadeghi, and L. B. Pedersen, 2015, Joint inversion of gravity, magnetic, and petrophysical data: A case study from a gabbro intrusion in Boden, Sweden: Geophysics, **80**, no. 5, B13–B152, doi: 10.1190/GEO2014-0122.1.

Kwok, Y. K., 1991, Gravity gradient tensors due to a polyhedron with polygonal facets: Geophysical Prospecting, **39**, 435–443, doi: 10.1111/j.1365-2478.1991.tb00320.x.

Lelièvre, P. G., 2003, Forward modeling and inversion of geophysical magnetic data: M.S. thesis, University of British Columbia.

Lelièvre, P. G., and D. W. Oldenburg, 2006, Magnetic forward modeling and inversion for high susceptibility: Geophysical Journal International, **166**, 76–90, doi: 10.1111/j.1365-246X.2006.02964.x.

Li, X., and M. Chouteau, 1998, Three-dimensional gravity modeling in all space: Survey in Geophysics, **19**, 339–368, doi: 10.1023/A:1006554408567.

Li, Y., and D. W. Oldenburg, 1996, 3-D inversion of magnetic data: Geophysics, **61**, 394–408, doi: 10.1190/1.1443968.

Li, Y., and D. W. Oldenburg, 1998, 3-D inversion of gravity data: Geophysics, **63**, 109–119, doi: 10.1190/1.1444302.

Maag, E., J. Capriotti, and Y. Li, 2017, 3D gravity inversion using the finite element method: 87th Annual International Meeting, SEG, Expanded Abstracts, 1713–1717, doi: 10.1190/segam2017-17682714.1.

Mosher, C. R. W., and C. G. Farquharson, 2013, Minimum-structure borehole gravity inversion for mineral exploration: A synthetic modeling study: Geophysics, **78**, no. 2, G25–G39, doi: 10.1190/GEO2012-0373.1.

Nabighian, M. N., V. J. S. Grauch, R. O. Hansen, T. R. Lafehr, Y. Li, J. W. Peirce, J. D. Phillips, and M. E. Ruder, 2005, The historical development of the magnetic method in exploration: Geophysics, **70**, no. 6, 33ND–61ND, doi: 10.1190/1.2133784.

Nagy, D., 1966, The gravitational attraction of a right rectangular prism: Geophysics, **31**, 362–371, doi: 10.1190/1.1439779.

Nagy, D., G. Papp, and J. Benedek, 2000, The gravitational potential and its derivatives for the prism: Journal of Geodesy, **74**, 552–560, doi: 10.1007/s001900000116.

Okabe, M., 1979, Analytical expressions for gravity anomalies due to homogeneous polyhedral bodies and translations into magnetic anomalies: Geophysics, **44**, 730–741, doi: 10.1190/1.1440973.

Parker, R. L., 1972, The rapid calculation of potential anomalies: Geophysical Journal International, **31**, 447–455, doi: 10.1111/j.1365-246X.1973.tb06513.x.

Paul, M. K., 1974, The gravity effect of a homogeneous polyhedron for three-dimensional interpretation: Pure and Applied Geophysics, **112**, 553–561, doi: 10.1007/BF00877292.
Pedersen, L. B., 1978a, A statistical analysis of potential fields using a vertical circular cylinder and a dike: Geophysics, **43**, 943–953, doi: 10.1016/0016-7142(78)90041-8.
Pedersen, L. B., 1978b, Wavenumber domain expressions for potential fields from arbitrary 2-, 21/2-, and 3-dimensional bodies: Geophysics, **43**, 626–630, doi: 10.1190/1.1440841.
Pedersen, L. B., 1985, The gravity and magnetic fields from ellipsoidal bodies in the wavenumber domain: Geophysical Prospecting, **33**, 263–281, doi: 10.1111/j.1365-2478.1985.tb00434.x.
Pedersen, L. B., and M. Bastani, 2016, Estimating rock-vector magnetization from coincident measurements of magnetic field and gravity gradient tensor: Geophysics, **81**, no. 3, B55–B64, doi: 10.1190/GEO2015-0100.1.
Phillips, J. D., F. Caratori Tontini, and L. Cocchi, 2008, Potential-field forward modeling and inversion using 3D fast Fourier transforms: AGU Fall Meeting Abstract, 89, 1.
Plouff, D., 1976, Gravity and magnetic fields of polygonal prisms and application to magnetic terrain corrections: Geophysics, **41**, 727–741, doi: 10.1190/1.1440645.
Prutkina, I., and A. Salehb, 2009, Gravity and magnetic data inversion for 3D topography of the Moho discontinuity in the northern Red Sea area, Egypt: Journal of Geodynamics, **47**, 237–245, doi: 10.1016/j.jog.2008.12.001.
Rao, D. B., M. J. Prakash, and N. R. Babu, 1993, Gravity interpretation using Fourier-transforms and simple geometrical models with exponential density: Geophysics, **58**, 1074–1083, doi: 10.1190/1.1443491.
Ren, Z., C. Chen, K. Pan, T. Kalscheuer, H. Maurer, and J. Tang, 2017a, Gravity anomalies of arbitrary 3D polyhedral bodies with horizontal and vertical mass contrasts: Survey in Geophysics, **38**, 479–502, doi: 10.1007/s10712–016-9395-x.
Ren, Z., J. Tang, T. Kalscheuer, and H. Maurer, 2017b, Fast 3-D large-scale gravity and magnetic modeling using unstructured grids and an adaptive multilevel fast multipole method: Journal of Geophysical Research: Solid Earth, **122**, 79–109, doi: 10.1002/2016JB012987.
Ren, Z., Y. Zhong, C. Chen, J. Tang, and K. Pan, 2018, Gravity anomalies of arbitrary 3D polyhedral bodies with horizontal and vertical mass contrasts up to cubic order: Geophysics, **83**, no. 1, G1–G13, doi: 10.1190/geo2017-0219.1.
Rim, H., and Y. Li, 2012, Single-hole imaging using borehole gravity gradiometry: Geophysics, **77**, no. 5, G67–G76, doi: 10.1190/GEO2012-0003.1.
Saleh, S., T. Jahr, G. Jentzsch, A. Saleh, and N. M. A. Ashour, 2006, Crustal evaluation of the northern red sea rift and Gulf of Suez, Egypt from geophysical data: 3-dimensional modeling: Journal of African Earth Sciences, **45**, 257–278, doi: 10.1016/j.jafrearsci.2006.02.001.
Singh, B., and D. Guptasarma, 2001, New method for fast computation of gravity and magnetic anomalies from arbitrary polyhedra: Geophysics, **66**, 521–526, doi: 10.1190/1.1444942.
Singh, S. K., and F. J. Sabina, 1978, Magnetic anomaly due to a vertical right circular cylinder with arbitrary polarization: Geophysics, **43**, 173–178, doi: 10.1190/1.1440818.
Talwani, M., 1960, Rapid computation of gravitational attraction of three-dimensional bodies of arbitrary shape: Geophysics, **25**, 203–225, doi: 10.1190/1.1438687.
Temperton, C., 1975, Algorithms for the solution of cyclic tridiagonal systems: Journal of Computational Physics, **19**, 317–323, doi: 10.1016/0021-9991(75)90081-9.
Tontini, F. C., L. Cocchi, and C. Carmisciano, 2009, Rapid 3-D forward model of fields with application to the Palinuro seamount gravity anomaly (Sourthern Tyrrhenian Sea, Italy): Journal of Geophysical Research: Solid Earth, **114**, 1205–1222, doi: 10.1029/2008JB005907.
Ward, S. H., and G. W. Hohmann, 1988, Electromagnetic theory for geophysical applications, *in* M. N. Nabighian, ed., Electromagnetic methods in applied geophysics: SEG, 131–311.
Wu, L., and L. Chen, 2016, Fourier forward modeling of vector and tensor gravity fields due to prismatic bodies with variable density contrast: Geophysics, **81**, no. 1, G13–G26, doi: 10.1190/GEO2014–0559.1.
Wu, L., and G. Tian, 2014, High-precision Fourier forward modeling of potential field: Geophysics, **79**, no. 5, G59–G68, doi: 10.1190/GEO2014-0039.1.
Wu, L. Y., 2016, Efficient modeling of gravity effects due to topographic masses using the Gauss-FFT method: Geophysical Journal International, **205**, 160–178, doi: 10.1093/gji/ggw010.
Wu, X. Z., 1983, The computation of spectrum of potential field due to 3-D arbitrary bodies with physical parameters varying with depth (in Chinese): Chinese Journal of Geophysics, **26**, 177–187.
Xiong, G. C., 1984, Some problems about 3-D Fourier transforms of the gravity and magnetic fields (in Chinese): Chinese Journal of Geophysics, **1**, 103–109.
Xu, S. Z., 1994, The finite element method in geophysics: Science Press.
Zhang, J., and L. Jiang, 2017, Analytical expressions for the gravitational vector field of a 3-D rectangular prism with density varying as an arbitrary-order polynomial function: Geophysical Journal International, **210**, 1176–1190, doi: 10.1093/gji/ggx230.
Zhao, G., B. Chen, L. Chen, J. Liu, and Z. Ren, 2018, High-accuracy 2D and 3D Fourier forward modeling of gravity field based on the Gauss-FFT method: Journal of Applied Geophysics, **150**, doi: 10.1016/j.jappgeo.2018.01.002.
Zhao, S. K., and M. J. Yedlin, 1991, Chebyshev expansions for the solution of the forward gravity problem: Geophysical Prospecting, **39**, 783–802, doi: 10.1111/j.1365-2478.1991.tb00344.x.
Zunino, A., F. Benvenuto, E. Armadillo, M. Bertero, and E. Bozzo, 2009, Iterative deconvolution and semiblind deconvolution methods in magnetic archaeological prospecting: Geophysics, **74**, no. 4, L43–L51, doi: 10.1190/3129263.